Performance of 3-D Surface Deformation Estimation for Simultaneous Squinted SAR Acquisitions

Prats-Iraola, Pau; Lopez-Dekker, Paco; De Zan, Francesco; Yague-Martinez, Nestor; Zonno, Mariantonietta; Rodriguez-Cassola, Marc

DOI
10.1109/TGRS.2017.2776140

Publication date
2018

Document Version
Accepted author manuscript

Published in
IEEE Transactions on Geoscience and Remote Sensing

Performance of 3-D Surface Deformation Estimation for Simultaneous Squinted SAR Acquisitions

Pau Prats-Iraola, *Senior Member, IEEE*, Paco Lopez-Dekker, *Senior Member, IEEE*, Francesco De Zan, Nestor Yague-Martinez, Mariantonietta Zonno, Marc Rodriguez-Cassola

***Abstract*—This paper addresses the performance in the retrieval of 3-D mean deformation maps by exploiting simultaneous or quasi-simultaneous squinted synthetic aperture radar (SAR) interferometric acquisitions in a repeat-pass scenario. In multi-satellite or multi-beam low Earth observation (LEO) missions the availability of two (or more) lines of sight allows the simultaneous acquisition of SAR images with different squint angles, hence improving the sensitivity to the north-south component of the deformation. Due to the simultaneity of the acquisitions, the troposphere will be highly correlated and, therefore, will tend to cancel out when performing the differential measurement between the interferograms obtained with the different lines of sight, hence resulting in a practically troposphere-free estimation of the along-track deformation measurement. In practice, though, the atmospheric noise in the differential measurement will increase for increasing angular separations. The present contribution expounds the mathematical framework to derive the performance by properly considering the correlation of the atmospheric delays between the simultaneous acquisitions. To that aim, the hybrid Cramér-Rao bound is exploited making use of the autocorrelation function of the troposphere. Some performance examples are presented in the frame of future spaceborne SAR missions at C- and L-band.**

***Index Terms*—Synthetic aperture radar (SAR), differential SAR interferometry (DInSAR), hybrid Cramér-Rao bound, squinted SAR acquisitions, troposphere, atmospheric boundary layer.**

I. Introduction

Differential synthetic aperture radar interferometry (DInSAR) is a well established technique that allows the accurate retrieval of the motion in the scene projected onto the line-of-sight (LOS) direction of the sensor with an accuracy proportional to the wavelength. Current low Earth orbit (LEO) spaceborne SAR missions exploit the repeated acquisition over the same area to build image stacks and retrieve the temporal evolution of the deformation for the scatterers in the scene that remain coherent in time. The combination of ascending and descending measurements further allows the inversion of the measurements from LOS to a local 3-D coordinate system [1]. In practice, however, the sensitivity to the north-south (N-S) component of the motion is very limited due to the near-polar orbits used by current spaceborne SAR missions.

The exploitation of squinted geometries to increase the sensitivity to the N-S direction has already been discussed in several papers [2]–[5], and has been also compared to the combination of opposite looking measurements [6]. This paper addresses the performance in the retrieval of the 3-D deformation map for the particular case where at least two simultaneous or quasi-simultaneous acquisitions with different squint angles (lines of sight) over the same area are available. That would be the case, for example, for multi-satellite spaceborne SAR missions currently under investigation like Tandem-L [7], SAOCOM-CS [8] or a companion satellite for Sentinel-1 [9]; or in the case of single-platform satellites with multiple beams, e.g., dual-beam concept [2], [5] or bidirectional SAR [3], [4], [10]. On the one hand, the (quasi-)simultaneous acquisition implies that most of the turbulent part of the troposphere, one of the main limiting performance factors in DInSAR, will be highly correlated, and consequently, the subtraction of the two measurements will result in an almost troposphere-free measurement. This measure is indeed proportional to the along-track deformation, and therefore, to the N-S component of the motion. Furthermore, as shown in the paper, increasing the angular separation between the acquisitions does not increase the troposphere-related error significantly, so that with a proper selection of the squint angle a relatively good performance in the N-S direction when compared to the other two components (east and vertical) can be achieved.

The observation that the turbulent part of the troposphere cancels out for small angular separations has been stated by several authors [11], [12]. Furthermore, there is an obvious link of the present multi-satellite configuration with the spectral diversity (SD) [13] or multiple-aperture interferometry (MAI) [11] technique, where in this case two independent looks are obtained from the full resolution azimuth bandwidth, hence resulting in two independent lines of sight. The performance of the SD/MAI technique has been already addressed in [14]–[17], where the influence of the troposphere has been neglected, being a reasonable assumption due to the small angular range of the considered azimuth bandwidths. Note, however, that for increasing angular separations this assumption is no longer valid, and therefore a new mathematical framework is required in order to evaluate the asymptotic performance in such cases, which is the main contribution of this paper. Finally, note also that for large along-track separations between

Manuscript received xxxx; revised xxxx.

P. Prats-Iraola, F. De Zan, N. Yague-Martinez, M. Zonno and M. Rodriguez-Cassola are with the German Aerospace Center (DLR), Oberpfaffenhofen D-82234, Germany (e-mail: Pau.Prats@dlr.de).

P. Lopez-Dekker is with the Delft University of Technology, Kluyverweg 1, 2629 HS Delft, The Netherlands.

This work has been partially funded under ESA contract 40001090705/14/NL/FF/lf.

the satellites one cannot assume the SD/MAI measurement will be oriented in the azimuth direction. Instead, the full 3-D geometry must be properly considered, as presented through this contribution.

The mathematical derivation for the performance of the 3-D surface deformation estimation is based on the work by Monti Guarnieri and Tebaldini [18], [19], who exploit the Hybrid Cramér-Rao bound (HCRB) to derive the performance of the mean surface deformation velocity for one single line of sight when working with image stacks. With the HCRB it is possible to obtain the asymptotic performance taking into account the troposphere, which is modeled as a random variable. In the present paper, we further exploit the HCRB and extend the formulation in order to obtain the 3-D surface deformation performance considering the correlation of the troposphere between simultaneous squinted acquisitions.

The paper is organized as follows. Section II expounds the mathematical framework to derive the performance, where three different approaches are presented. This section includes also a discussion on the modeling of the turbulent part of the troposphere, including a quantitative analysis with TerraSAR-X interferometric data, as well as a comment on the processing strategy and the link of the presented rationale with the SD/MAI technique [11], [13]. Finally, Section III evaluates the performance for different mission scenarios and discusses the results.

II. 3-D Motion Retrieval Performance in Multi-Squinted Configurations

In the following, the Cramér-Rao bound (CRB) for the retrieval of the 3-D deformation maps with two or more simultaneous squints is expounded. The analysis focuses on distributed scatterers, where target decorrelation plays a critical role in the final performance. Section II-A makes the derivation for the particular case of two monostatic acquisitions. Section II-B extends the derivation to one monostatic and one bistatic acquisition, and finally Section II-C proposes a more general performance evaluation. Section II-D addresses the role of the atmosphere and characterizes the turbulent part of the troposphere in order derive the CRB. Section II-E comments on the link of the multi-squinted geometry with spectral diversity and finally Section II-F addresses the processing strategy in order to achieve the presented CRB.

A. Mathematical Derivation for the Monostatic Case

The following derivation assumes two satellites observing the scene quasi simultaneously and independently. For the sake of the example, the first satellite illuminates the scene in a zero-squinted geometry and the second satellite works in a squinted geometry as depicted in Fig. 1(right). The extension to the bistatic configuration of Fig. 1(left) is addressed in Section II-B, while the modification of the monostatic case for arbitrary squinted geometries, e.g., symmetric, is straightforward.

The observation geometries are defined by their unitary line of sight vectors, $\hat{e}_A$ and $\hat{e}_B$ for each satellite, respectively. Without loss of generality, these vectors are defined in a local

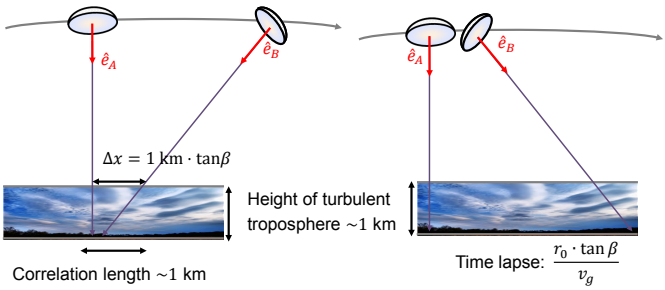

Fig. 1. Sketch of the different acquisition geometries under investigation. The atmospheric boundary layer, which has a height between 1 — 2 km, is highly correlated for the two squints (lines of sight). (Left) Simultaneous and (right) quasi-simultaneous acquisitions by using the bistatic and monostatic modes, respectively.

coordinate system with components east, north and vertical. The lines of sight are plotted in the 2-D sketch of Fig. 1 at the satellite level. We further assume in the following a repeat-pass scenario with acquisition times t_1 and t_2, where the two lines of sight A and B are being acquired quasi-simultaneously. Two interferograms can be formed, whose interferometric phases neglecting the topographic component are given by

$$\varphi_A = \frac{4\pi}{\lambda} \cdot [\langle \vec{x}, \hat{e}_A \rangle + \alpha_{A,t_1} - \alpha_{A,t_2}] + n_A \quad (1)$$

$$\varphi_B = \frac{4\pi}{\lambda} \cdot [\langle \vec{x}, \hat{e}_B \rangle + \alpha_{B,t_1} - \alpha_{B,t_2}] + n_B, \quad (2)$$

where $\vec{x}$ is the motion vector of the target, $\langle \cdot, \cdot \rangle$ represents the dot product, λ is the wavelength, the subscripts A and B indicate the geometries corresponding to the first and the second line of sight, respectively, the $\alpha_{\{A,B\},t_i}$ represent the one-way atmospheric range delays, and $n_{\{A,B\}}$ represents the phase noise. It is implicitly being assumed that the same resolution cell after the multilook operation (spatial averaging) has coherent information in each geometry, and that, even if the phase centers are different due to the different squinted geometries, they still undergo the same deformation. Note that in differential interferometry one is interested in the relative change of the phase center, and not in its absolute location. These assumptions are not necessarily valid in the case of permanent scatterer (PS) [20], since the larger the difference between the geometries, the smaller the PS has to be in the azimuthal direction in order to be observed by both, which directly implies a smaller signal-to-clutter ratio. Note, however, that in a urban scenario a large squint angle will offer the possibility to detect new PSs that are not observed in the other geometry [21], which on the other hand must not necessarily undergo the same deformation.

In order to derive the performance, we build an orthogonal system by generating two new interferograms with the sum and the difference of the original phases, namely,

$$\Delta\varphi_\Sigma = \varphi_A + \varphi_B = \frac{4\pi}{\lambda} \cdot [\langle \vec{x}, \hat{e}_A \rangle + \langle \vec{x}, \hat{e}_B \rangle + \alpha_{A,t_1} + \alpha_{B,t_1} - (\alpha_{A,t_2} + \alpha_{B,t_2})] + n_A + n_B \quad (3)$$

$$\Delta\varphi_\Delta = \varphi_A - \varphi_B = \frac{4\pi}{\lambda} \cdot [\langle \vec{x}, \hat{e}_A \rangle - \langle \vec{x}, \hat{e}_B \rangle + \alpha_{A,t_1} - \alpha_{B,t_1} - (\alpha_{A,t_2} - \alpha_{B,t_2})] + n_A - n_B \quad (4)$$

We evaluate then the power of the atmosphere for the correlated components in (3) and (4) as

$$\sigma^2_{\alpha,\Sigma} = E\left\{|\alpha_{A,t_i}+\alpha_{B,t_i}|^2\right\} = 2\cdot\left[R(0)+R(\Delta x)\right] \quad (5)$$

$$\sigma^2_{\alpha,\Delta} = E\left\{|\alpha_{A,t_i}-\alpha_{B,t_i}|^2\right\} = 2\cdot\left[R(0)-R(\Delta x)\right] \quad (6)$$

where $R(\,\cdot\,)$ represents the spatial autocorrelation function of the atmosphere assuming stationarity and Δx is the distance at which the autocorrelation function is evaluated and depends on the differential squint angle between the two acquisitions. It is easy to evaluate that the sum and difference interferograms are orthogonal both in terms of the scatterer phase noise and of the atmospheric signal, i.e., $E\{\Delta\varphi_\Sigma \cdot \Delta\varphi_\Delta\} = 0$.

From (5) and (6) it is clear that the amount of atmospheric power depends on the spatial autocorrelation function. As shown later in Section II-D, the contribution due to the turbulent part of the troposphere will be highly correlated, hence cancelling out almost completely in the difference interferogram. Note further that the difference of phases is practically only sensitive to the along-track component of the motion, which for typical low Earth orbit (LEO) satellite missions with near-polar orbits is mainly sensitive to the N-S direction. On the other hand, the sum of the phases is sensitive mainly to the across-track motion, i.e., east-west and vertical components. Therefore, it is now clear that with (quasi-)simultaneous squinted acquisitions the measurement of the N-S motion component will benefit from the high correlation of the atmospheric delays between the two lines of sight.

Considering now a stack of images (one for the sum and one for the difference), the Fisher information matrix (FIM) related to the scatterer phase information within each stack is given by [19]

$$\mathbf{X}_{\{\Sigma,\Delta\}} = N\cdot\left(\mathbf{\Gamma}_i \odot \mathbf{\Gamma}_i^{-1} - \mathbf{I}\right), \quad (7)$$

where N is the number of independent averaged samples, $\mathbf{\Gamma}_i$ is the covariance matrix of all possible interferograms, $\mathbf{I}$ is the identity matrix and $\odot$ represents the Hadamard product (entry-wise). Note that the variable i is used to indicate different covariance matrices for the sum and the difference. The missing factor 2 w.r.t. the equation shown in [18], [19] is due to the fact that the phase noise increased when performing the sum and the difference of the phases. Afterwards, the Hybrid Cramér-Rao bound (HCRB) [18], [19] can be applied to the sum and the difference image stacks independently in order to retrieve the performance. For completeness, the solution is shown in the following. The hybrid Fisher Information matrix is given by

$$\mathbf{J}_{\{\Sigma,\Delta\}} = \begin{bmatrix} \mathbf{t}^T\mathbf{X}_i\mathbf{t} & \mathbf{t}^T\mathbf{X}_i \\ \mathbf{X}_i\mathbf{t} & \mathbf{X}_i + \sigma_i^{-2}\mathbf{I} \end{bmatrix} \quad (8)$$

where $\mathbf{t}$ is the vector containing the acquisition times in days, $\mathbf{X}_i$ comes from (7) and the power of the atmospheric delays, σ_i^2, for the sum and the difference are given by (5) and (6), respectively. The first element of the inverse of $\mathbf{J}$ contains the Cramér-Rao bound of the deformation velocity in units radians per day, indicated as σ^2_Σ and σ^2_Δ for the sum and the difference, respectively.

Once the time series HCRB for the sum and difference lines of sight has been obtained, one can evaluate the performance in the retrieval of the deformation in a local 3-D coordinate system by combining ascending and descending geometries. Having a set of M geometries (lines of sight), the system of equations is given by [1], [6]

$$\begin{aligned} \mathbf{y} &= \mathbf{K}\mathbf{x} \\ \begin{bmatrix}\Delta r_1 \\ \vdots \\ \Delta r_{\mathrm{M}}\end{bmatrix} &= \begin{bmatrix}\hat{e}_{e,1} & \hat{e}_{n,1} & \hat{e}_{v,1} \\ \vdots & \vdots & \vdots \\ \hat{e}_{e,\mathrm{M}} & \hat{e}_{n,\mathrm{M}} & \hat{e}_{v,\mathrm{M}}\end{bmatrix}\begin{bmatrix}x_e \\ x_n \\ x_v\end{bmatrix}, \end{aligned} \quad (9)$$

with the subscripts e, n, v indicating the easting, northing and vertical components, respectively. The 3-D motion vector can be retrieved using a weighted least-squares (WLS) approach, where the achievable accuracy is bounded by the diagonal elements of the matrix

$$\mathbf{P} = (\mathbf{K}^T\mathbf{W}\mathbf{K})^{-1}, \quad (10)$$

where the weights in the matrix $\mathbf{W}$ are computed as the inverse of the variances obtained after applying the HCRB in the previous step. Following the same example as before, with two monostatic acquisitions and having one ascending pass and one descending pass, the $\mathbf{K}$ and $\mathbf{W}$ matrices would be given by

$$\mathbf{K} = \frac{4\pi}{\lambda}\begin{bmatrix}\hat{e}_{A,Asc}+\hat{e}_{B,Asc} \\ \hat{e}_{A,Asc}-\hat{e}_{B,Asc} \\ \hat{e}_{A,Desc}+\hat{e}_{B,Desc} \\ \hat{e}_{A,Desc}-\hat{e}_{B,Desc}\end{bmatrix} \quad (11)$$

$$\mathbf{W} = \mathrm{diag}\{1/\sigma^2_{\Sigma,Asc}, 1/\sigma^2_{\Delta,Asc}, 1/\sigma^2_{\Sigma,Desc}, 1/\sigma^2_{\Delta,Desc}\}, \quad (12)$$

being $\mathbf{W}$ a diagonal matrix, for the system has been orthogonalized. The above equations are only valid for the monostatic case, where the sum and the difference of the original phases allows for a straightforward orthogonalization of the system. However, in the bistatic case such approach will not work, as the sum and the difference measurements are indeed correlated in terms of atmospheric signal. The next section derives the CRB for this more general case.

B. Mathematical Derivation for the Bistatic Case

This section derives the Cramér-Rao bound for the case where one of the acquisitions is bistatic, as depicted in Fig. 1(left), and it is assumed that an exact time and phase synchronization of the bistatic image has been performed. Since it is not possible to orthogonalize the system as in the monostatic case, one has to derive the CRB considering the two lines of sight simultaneously. We propose to define two orthogonal vectors in the slant-range plane of the master satellite and to compute the performance in the estimation of the velocity for each of the directions indicated by these two vectors. Without loss of generality, we select the slant-range plane containing the line of sight of the monostatic acquisition, which in our example is zero-squinted, so that the two orthogonal vectors are given by $\hat{e}_A$ and $\hat{v}_A$, being the latter the normalized velocity vector, and both are given

at the zero-Doppler position of the target. We then define the deformation velocities to be estimated as v_r and v_a for range and azimuth, respectively. In this new coordinate system, the unitary vectors for master and slave are given by

$$\hat{e}_{SR,A}^T = [1,0] \quad (13)$$

$$\hat{e}_{SR,B}^T = [\langle \hat{e}_A, \hat{e}_B \rangle, \langle \hat{v}_A, \hat{e}_B \rangle] \quad (14)$$

with the subscript SR indicating the slant-range plane. The hybrid Fisher Information matrix has the form [22]

$$\mathbf{J} = \mathbf{J}_D + \mathbf{J}_R \quad (15)$$

where $\mathbf{J}_D$ represents the Fisher information matrix of the deterministic unknowns, i.e., the velocities, while $\mathbf{J}_R$ is related to the random variables, i.e., the atmospheric delays in our case. The elements are defined as [18], [22], [23]

$$[J_D]_{ij} = -E_{\mathbf{y},\boldsymbol{\theta}} \left[\frac{\partial^2 \ln p(\mathbf{y}/\boldsymbol{\theta})}{\partial \theta_i \partial \theta_j} \right] \quad (16)$$

$$[J_R]_{ij} = -E_{\boldsymbol{\theta}} \left[\frac{\partial^2 \ln p(\boldsymbol{\theta})}{\partial \theta_i \partial \theta_j} \right] \quad (17)$$

where $p(\mathbf{y}/\boldsymbol{\theta})$ is the conditional probability function of the data vector $\mathbf{y}$ for a given parameter vector $\boldsymbol{\theta}$, and $p(\boldsymbol{\theta})$ is the prior probability density of $\boldsymbol{\theta}$. The parameter vector is given by

$$\boldsymbol{\theta} = (v_r, v_a, \rho_{A,t_1}, \ldots, \rho_{A,t_M}, \rho_{B,t_1}, \ldots, \rho_{B,t_M}), \quad (18)$$

where the ρ parameters correspond to the contribution of the atmosphere in radians.

Considering the interferometric SAR data statistics (see [18], [19] for the details), and that the atmospheric delays have a zero mean Gaussian distribution, it follows that the matrices $\mathbf{J}_D$ and $\mathbf{J}_R$ are given by

$$\mathbf{J}_D = \begin{bmatrix} \sum_{k,p} \mathbf{q}^T \mathbf{X}_p \mathbf{q} \cdot \hat{e}_k \hat{e}_k^T & \hat{e}_1 \mathbf{q}^T \mathbf{X}_A & \hat{e}_2 \mathbf{q}^T \mathbf{X}_B \\ \mathbf{X}_A \mathbf{q} \hat{e}_1^T & \mathbf{X}_A & 0 \\ \mathbf{X}_B \mathbf{q} \hat{e}_2^T & 0 & \mathbf{X}_B \end{bmatrix} \quad (19)$$

$$\mathbf{J}_R = \begin{bmatrix} 0_{2\times 2} & 0_{2\times 2L} \\ 0_{2L\times 2} & \mathbf{J}_{R,\text{sub}} \end{bmatrix} \quad (20)$$

$$\mathbf{J}_{R,\text{sub}} = \begin{bmatrix} \mathbf{V}_0 & \mathbf{V}_{\Delta x} \\ \mathbf{V}_{\Delta x} & \mathbf{V}_0 \end{bmatrix}^{-1} \quad (21)$$

where $k = \{1,2\}$ and $p = \{A,B\}$, $\mathbf{q}$ is the vector containing the acquisition times scaled with $4\pi/\lambda$, which due to the simultaneous acquisition is the same for both A and B geometries, L represents the number of available images in the stack for each line of sight, and $\mathbf{e}$ is a 2×2 matrix containing the unitary lines of sight vectors in the slant-range plane. For the bistatic case, this matrix has the form

$$\mathbf{e} = \begin{bmatrix} \hat{e}_1^T \\ \hat{e}_2^T \end{bmatrix} = \begin{bmatrix} \hat{e}_{SR,A}^T \\ \dfrac{\hat{e}_{SR,A}^T + \hat{e}_{SR,B}^T}{2} \end{bmatrix}. \quad (22)$$

$\mathbf{X}$ represents the Fisher information matrix of the scatterer phases given by [18], [19]

$$\mathbf{X}_k = 2N \cdot \left(\boldsymbol{\Gamma}_k \odot \boldsymbol{\Gamma}_k^{-1} - \mathbf{I} \right). \quad (23)$$

The term $\mathbf{J}_R$ in (21) has been derived based on the following identity [18], [22]

$$\mathbf{J}_{R,\text{sub}} = \boldsymbol{\Lambda}_\alpha^{-1} \quad (24)$$

where $\boldsymbol{\Lambda}_\alpha$ is the covariance matrix of the random parameters, i.e., the atmospheric delays. The $L \times L$ submatrix $\mathbf{V}_0$ represents the power of the atmospheric delays in radians and is therefore a diagonal matrix where each entry is equal to

$$V_{0,ii} = \left(\frac{4\pi}{\lambda} \right)^2 \cdot R(0). \quad (25)$$

The $L \times L$ submatrix $\mathbf{V}_{\Delta x}$ indicates the amount of correlation in the atmospheric signal between the two lines of sight and is therefore again diagonal. The amount of correlation for the slave interferogram in the bistatic case is given by

$$E\left\{ \alpha_A \cdot \frac{(\alpha_A + \alpha_B)}{2} \right\} = \frac{R(0) + R(\Delta x)}{2}, \quad (26)$$

so that each diagonal element of $\mathbf{V}_{\Delta x}$ is given by

$$V_{\Delta x,ii} = \left(\frac{4\pi}{\lambda} \right)^2 \cdot \left(\frac{R(0) + R(\Delta x)}{2} \right). \quad (27)$$

The upper left 2×2 submatrix of $\mathbf{J}^{-1}$ contains the desired Cramér-Rao bound for the estimation of the v_r and v_a deformation velocities.

Similar as in the previous section, the 3-D achievable accuracy can be computed for all available geometries in a second step by using eq. (10). For the case of one ascending and one descending geometry, the matrices $\mathbf{K}$ and $\mathbf{W}$ would be given by

$$\mathbf{K}^T = [\hat{e}_{A,Asc}, \hat{v}_{A,Asc}, \hat{e}_{A,Desc}, \hat{v}_{A,Desc}] \quad (28)$$

$$\mathbf{W} = \begin{bmatrix} \{\mathbf{J}_{Asc}^{-1}\}_{UL,2\times 2} & 0_{2\times 2} \\ 0_{2\times 2} & \{\mathbf{J}_{Desc}^{-1}\}_{UL,2\times 2} \end{bmatrix}^{-1}, \quad (29)$$

where the subscript $UL, 2 \times 2$ indicates the upper left submatrix, and note that the $4\pi/\lambda$ factor has been omitted when compared to (11) as it is already included in the $\mathbf{q}$ vector. The diagonal elements of $\mathbf{P}$ contain the CRB of the velocity estimates in the 3-D coordinate system.

The formulation shown in this section includes the monostatic case by simply using the proper vectors in (22) and considering the appropriate correlations in (27). Furthermore, it is also straightforward to extend the formulation for the case where more than two simultaneous lines of sight are available, as it would be the case of a multi-static mission.

C. Mathematical Derivation for the Generic Case

The two previous sections have derived the CRB in a two-step approach. First, the HCRB has been exploited to derive the performance in the slant-range plane, and, in a second step, the 3-D performance has been obtained by using all the available geometries using the conventional weighted least squares with the covariances derived in the first step. While the formulation presented for the bistatic case (Section II-B) is already generic and can be applied to any configuration, the current section presents the equations to retrieve the performance in one single step.

Indeed, similar as done with equations (19) and (21), it is straightforward to obtain the $\mathbf{J}_D$ and $\mathbf{J}_R$ matrices for deriving the performance in a local 3-D coordinate system as

$$\begin{aligned}
\mathbf{J}_D &= \begin{bmatrix} \sum_k \mathbf{q}_k^T \mathbf{X}_k \mathbf{q}_k \cdot \hat{e}_k \hat{e}_k^T & \hat{e}_1 \mathbf{q}_1^T \mathbf{X}_1 & \dots & \hat{e}_M \mathbf{q}_M^T \mathbf{X}_M \\ \mathbf{X}_1 \mathbf{q}_1 \hat{e}_1^T & \mathbf{X}_1 & 0 & 0 \\ \vdots & 0 & \ddots & 0 \\ \mathbf{X}_M \mathbf{q}_M \hat{e}_M^T & 0 & 0 & \mathbf{X}_M \end{bmatrix} \\
\mathbf{J}_R &= \begin{bmatrix} 0_{3\times 3} & 0_{3\times ML} \\ 0_{ML\times 3} & \mathbf{J}_{R,\text{sub}} \end{bmatrix} \\
\mathbf{J}_{R,sub} &= \begin{bmatrix} \mathbf{V}_0 & \mathbf{V}_{\Delta x} & \dots & 0 & 0 \\ \mathbf{V}_{\Delta x} & \mathbf{V}_0 & \dots & 0 & 0 \\ \vdots & \vdots & \ddots & \vdots & \vdots \\ 0 & 0 & \dots & \mathbf{V}_0 & \mathbf{V}_{\Delta x} \\ 0 & 0 & \dots & \mathbf{V}_{\Delta x} & \mathbf{V}_0 \end{bmatrix}^{-1},
\end{aligned} \tag{30}$$

where now the unitary vectors are three dimensional and $\mathbf{q_k}$ and $\mathbf{X}_k$ are defined as in the previous section. $\mathbf{J}_R^{-1}$ has been represented assuming that the geometries with correlated atmospheric delays have been placed contiguously in the matrix. As in the previous section, the effective bistatic lines of sight are given by the average of the master and slave unitary line of sight vectors. Eventually, the upper left 3×3 submatrix of the inverse matrix $\mathbf{J}^{-1}$ is the Cramér-Rao bound for the velocity estimates in the 3-D coordinate system.

D. Atmospheric Modeling

In this section we address the modeling of the atmosphere for the purpose of evaluating its autocorrelation function in order to compute the performance presented in the previous section. As shown in several references, the atmospheric refractivity can be decomposed in the hydrostatic, wet, ionospheric and liquid terms [24]. As generally accepted in the literature, the hydrostatic term can be assumed to be almost time invariant, being highly correlated with the topography. Furthermore, this term has a smooth behavior due to the large spatial scale of low and high pressure fields [24], and therefore will be highly correlated even for high tropospheric altitudes and for large differences of squint angles. Similarly, the liquid term is also ignored in the following. On the contrary, the wet term is the one that has a higher spatial variability and is responsible for the atmospheric artifacts that can be observed in SAR interferograms. The exploitation of SAR image stacks is usually required in order to mitigate the impact of this atmospheric phase screen (APS) in the retrieval of the deformation time series [25]. The portion of the troposphere responsible for this turbulence is called the atmospheric boundary layer (ABL) in atmospheric research, and is located in the lower troposphere with heights between $1-2\,\mathrm{km}$ [26]. Furthermore, its spatial correlation length in the horizontal plane is in the same order as the layer height, as depicted in Fig. 1.

The power spectrum of the ABL can be modeled following Kolmogorov's power law in the form $1/f^{\beta}$, where in the two-dimensional case $\beta \approx -8/3$ [24], [27]. Fig. 2 shows the power spectral density function (PSD) and the corresponding autocorrelation function for a signal power of $1\,\mathrm{cm}^2$. From

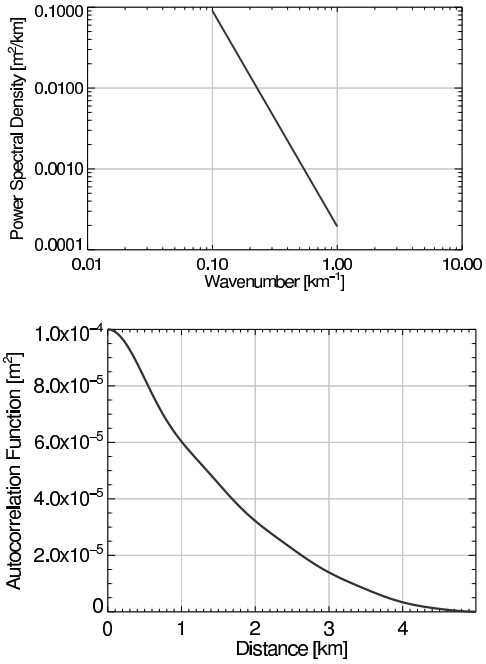

Fig. 2. (Top) Simulated power spectral density function profile (for $k_y = 0$) for the ABL following a power law and (bottom) its corresponding autocorrelation function profile after the 2D inverse Fourier transform. A tropospheric power of $1\,\mathrm{cm}^2$ has been used.

the latter, it is clear that even for significant squint angles the APS will be highly correlated. For example, squint angles of $10^\circ - 20^\circ$ correspond to a Δx of $176 - 363\,\mathrm{m}$ for an ABL height of $1\,\mathrm{km}$. The assumption of taking the maximum height of the ABL is indeed the worst case, since the effective height will be in general lower than that. In addition, one should further consider the fact that the transmitted signals converge as they get closer to the ground, which further improves the correlation of the observed tropospheric delays. In the simulations of Section III an effective height of $700\,\mathrm{m}$ for the ABL has been considered.

In the case of quasi-simultaneous acquisitions, e.g., with two monostatic surveys as sketched in Fig. 1(right), one should consider the time lapse between the two acquisitions when illuminating the same target on ground, since the turbulent part of the troposphere might have moved between acquisitions. Therefore, under the assumption of Taylor's frozen turbulence hypothesis [28], in the worst case the Δx for the computation of the troposphere power should be updated with an additional contribution due to the boundary layer motion given by

$$\delta x = \frac{r_0 \cdot \tan\beta}{v_g} v_{bl}, \tag{31}$$

where r_0 is the zero-Doppler slant-range distance, β is the squint angle, v_g is the ground or footprint velocity, and v_{bl} is the mean effective horizontal velocity of the turbulent flow within the boundary layer.

Finally, the ionospheric term needs to be also addressed, which is especially relevant for lower frequencies like L-band or P-band. Indeed, due to the higher altitude of the ionosphere and its properties, it can no longer be assumed that the two simultaneous observation geometries will observe correlated

ionospheric screens. While that might be the case for very small squint angles, it will be shown later that larger squint angles are required to achieve a reasonable accuracy in the retrieval of the motion in the N-S direction. Therefore, when computing the HCRB, one should also consider the influence of uncorrelated ionospheric components for the two lines of sight. A more detailed analysis on the spatial autocorrelation of the ionosphere (namely, the total electron content, TEC) would be required, which could be likewise included in the performance analysis as done with the turbulent part of the troposphere. For the numerical evaluation in Section III the ionosphere will be assumed uncorrelated between the simultaneous acquisitions.

Note that existing techniques for the estimation and correction of ionospheric effects can achieve accuracies better than $1\,\mathrm{cm}$ when averaging over an area of $1\,\mathrm{km}^2$ [29]. For the spatially low frequency components of the ionosphere, which are in general the most dominant, the performance in the estimation of the ionospheric artifacts can be improved by increasing the averaging window. Furthermore, the impact of these low frequency components will not be significant in relative terms at local scales. Note that in most scenarios residual trends are usually estimated and removed by the processing chain.

The lack of real data acquired with simultaneous squints does not allow for a full evaluation of the considered assumptions related to the ABL. However, in the following a representative analysis with TerraSAR-X staring spotlight (ST) data is shown in order to proof the point, at least as much as the data allow for it. The ST mode has a nominal azimuth resolution of $16\,\mathrm{cm}$ without spectral weighting [30], [31], which corresponds to an azimuth integration angle of about $4.4°$. Therefore, with a repeat-pass interferometric ST pair it is possible to evaluate the SD/MAI phase for different angular separations up to approximately $4.4°$. In the present case, several sub-look pairs of $1\,\mathrm{kHz}$ Doppler bandwidth have been generated, and their separation has been increased up to the maximum possible. For each sub-look pair, the SD/MAI phase has been computed by performing the following operation [13]

$$\varphi_{\mathrm{SD}} = \arg\left\{\left(\, s_{1,u}\cdot s_{2,u}^{*}\,\right)\cdot\left(\, s_{1,l}\cdot s_{2,l}^{*}\,\right)^{*}\right\} \tag{32}$$

with $s_{1,u}$ and $s_{2,u}$ being the upper sub-looks for image 1 and 2, respectively, and $s_{1,l}$ and $s_{2,l}$ the corresponding lower sub-looks. Fig. 3 shows the resulting analysis for two interferograms, one ascending and one descending, acquired over the city of Berlin, Germany, with a repeat-pass interval of eleven days (see Table I for further details). Both interferograms have very small perpendicular baselines: $19\,\mathrm{m}$ and $2\,\mathrm{m}$ for the ascending and descending interferograms, respectively. Consequently, but for a few differential effects in some buildings (e.g., Berlin's central train station), the low-pass phases that can be observed in the DEM-flattened interferograms can be solely attributed to atmospheric artifacts, and mainly to disturbances occurring at the ABL. The SD/MAI phases, on the other hand, show no residual tropospheric signatures for small angular separations, starting to be noticeable for the larger angular distances. It is also interesting to remark that the ascending configuration seems to have more tropospheric signal than the descending one, as in the TerraSAR-X mission the ascending acquisitions occur at dusk, where the ABL is usually more active.

From the signal processing point of view, the SD/MAI phases of the ST acquisitions are showing the derivative of the differential phase history along the synthetic aperture. Due to the spectral separation between sub-looks, this derivative is being sampled differently, being more sensitivity for larger separations between sub-looks, but also having a worse performance when tracking fast variations [32]. In the case of a differential phase ramp, as it would be the case for an azimuth displacement, the resulting SD/MAI phase would be the displacement scaled by the distance between the looks (see next Section). In a more generic case, however, one should be careful how to interpret the SD/MAI phase, as atmospheric disturbances can introduce higher-order terms along the synthetic aperture.

The conclusions derived from the images shown in Fig. 3 are further confirmed by their variograms in Fig. 4. In order to compute the variograms, a strong spatial averaging has been applied ($250\,\mathrm{m}\times250\,\mathrm{m}$), as we are only interested in the analysis of the low-pass component due to the ABL. Note also that a minimum coherence threshold of 0.5 has been used to randomly select the 10000 points for the computation of the variogram. The variograms clearly show that the SD/MAI phases have much less tropospheric signal. Note that due to the small image size of the ST acquisition mode, of about $6\mathrm{km}\times3\mathrm{km}$ (ground range$\times$azimuth), the variograms are only shown up to a distance of $2\,\mathrm{km}$, since for larger distances the results start not to be representative.

TABLE I
TERRASAR-X STARING SPOTLIGHT ACQUISITIONS

Parameter	Ascending	Descending
Perpendicular baseline	19.6 m	2.0 m
Master acq. date	2016-08-08	2016-07-30
Slave acq. date	2016-08-19	2016-08-10
Central frequency	9.65 GHz	
Azimuth bandwidth	38.2 kHz	
Range bandwidth	300 MHz	
Image size (ground range$\times$azimuth)	6 km$\times$3 km	

E. Link with the Spectral Diversity/MAI Technique

As mentioned in the introduction, it is worthwhile to remark the link of the differential phase measurement in (4) with the spectral diversity [aka split-spectrum aka multiple-aperture interferometry (MAI) aka split-bandwidth], technique [11], [13], [14] to measure the mutual shift between image pairs. As commented in [14], the exploitation of two azimuth sub-looks (lines of sight) is an approach to estimate the slope of the interferometric phase as a function of the Doppler frequency. Note that the interferometric phase at the maximum of the impulse response of the interferogram due to an azimuth shift is given by [11], [13], [33]

$$\varphi_{\mathrm{shift}} = 2\pi\cdot f_{\mathrm{DC}}\cdot\delta t = \frac{4\pi}{\lambda}\delta x\sin\beta, \tag{33}$$

where f_{DC} is the Doppler centroid, δt and δx represent the azimuth shift in seconds and meters, respectively, and β is

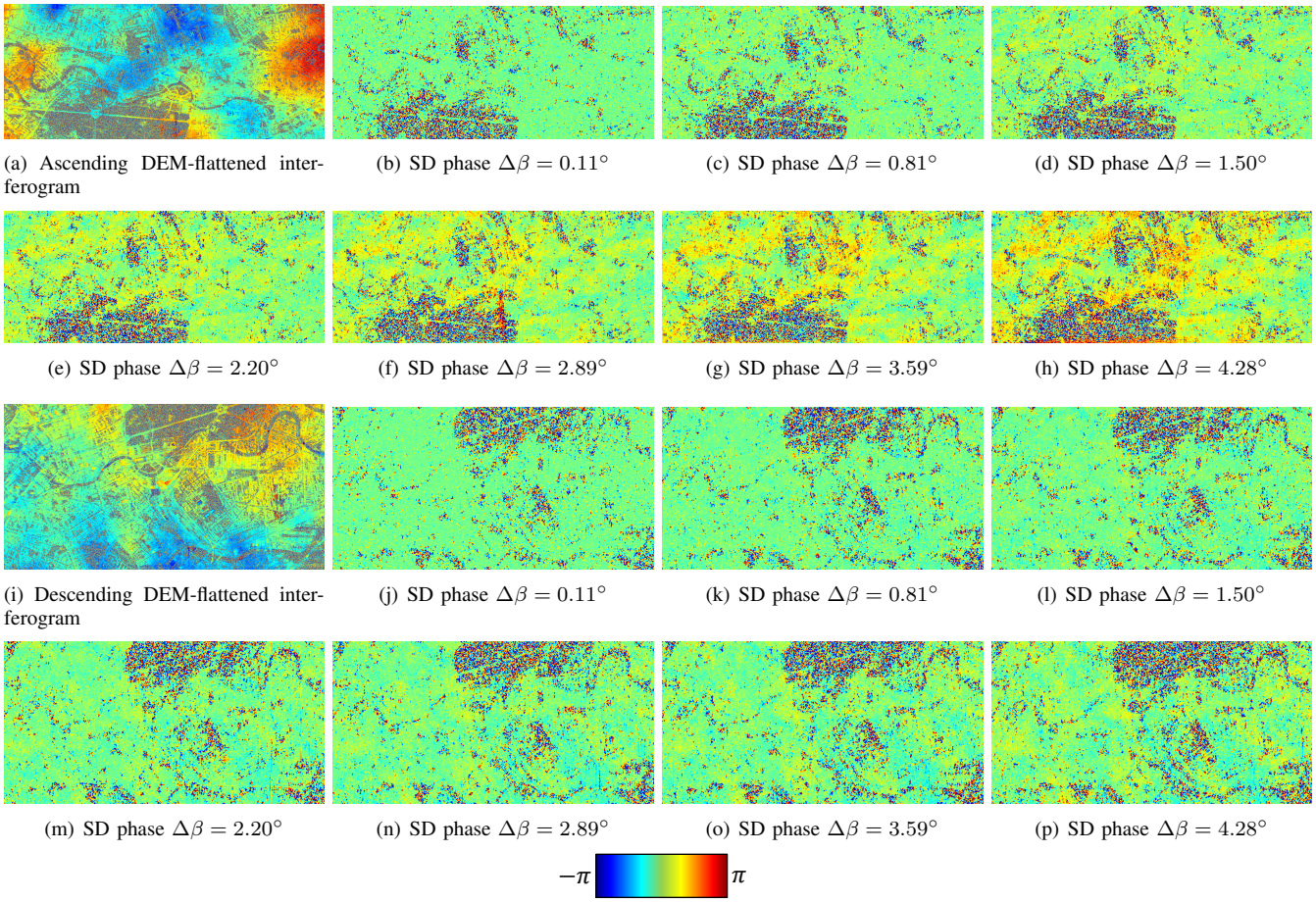

(a) Ascending DEM-flattened interferogram (b) SD phase $\Delta\beta = 0.11°$ (c) SD phase $\Delta\beta = 0.81°$ (d) SD phase $\Delta\beta = 1.50°$

(e) SD phase $\Delta\beta = 2.20°$ (f) SD phase $\Delta\beta = 2.89°$ (g) SD phase $\Delta\beta = 3.59°$ (h) SD phase $\Delta\beta = 4.28°$

(i) Descending DEM-flattened interferogram (j) SD phase $\Delta\beta = 0.11°$ (k) SD phase $\Delta\beta = 0.81°$ (l) SD phase $\Delta\beta = 1.50°$

(m) SD phase $\Delta\beta = 2.20°$ (n) SD phase $\Delta\beta = 2.89°$ (o) SD phase $\Delta\beta = 3.59°$ (p) SD phase $\Delta\beta = 4.28°$

Fig. 3. Evaluation of the tropospheric signal in the SD/MAI phases for two ST interferograms over Berlin, Germany, corresponding to (a)-(h) the ascending geometry and (i)-(p) the descending geometry. The original interferometric phases are shown in (a) and (i) for the ascending and the descending geometries, respectively. The remaining images show the SD/MAI phases for different angular separations, ranging from $\Delta\beta = 0.11°$ to $\Delta\beta = 4.28°$. Color scale between $-\pi$ (blue) and π (red). The conversion of the SD/MAI phases to meters (see Section II-E) results in the following scaling of the images: ± 353.2 cm [(b) and (j)], ± 50.4 cm [(c) and (k)], ± 27.1 cm [(d) and (l)], ± 18.5 cm [(e) and (m)],± 14.1 cm [(f) and (n)],± 11.3 cm [(g) and (o)], ± 9.5 cm [(h) and (p)]. Radar illumination from the left.

the effective squint angle under which the target is observed. Therefore, the azimuth shifts can be interpreted as phase slopes in the Doppler (or angular) domain. By taking two different looks and computing the differential interferogram, all Doppler-independent contributions will cancel out, so that for small angular separations, $\Delta\beta$, (or, equivalently, small Doppler separations, Δf) the azimuth shift will be given by

$$\delta x = \frac{\varphi_A - \varphi_B}{2\pi \cdot \Delta f} \cdot v_g \approx \frac{\lambda}{4\pi} \frac{\varphi_A - \varphi_B}{\Delta\beta}, \tag{34}$$

which is the original SD/MAI result [11], [13]. Consequently, the larger the separation between lines of sight, the better the sensitivity to the azimuth shift. However, one should also consider other sources introducing differential phase gradients, e.g., the differential ionosphere for spaceborne acquisitions [34], [35], time-varying baseline errors [12], [36], [37] or differential residual clock synchronization errors [38]. These additional phase gradients, if present, will be also sensed and therefore will bias the desired displacement measure unless they are estimated and removed, as already commented in the previous section.

As a final comment, note that eq. (34) is accurate for symmetric squint angles and small angular differences, where it is further assumed that the retrieved displacement is oriented in the along-track direction. However, for asymmetric squint angles or large angular separations as investigated in this paper, the true geometry using the line of sight vectors should be used to retrieve accurate measurements.

F. Comment on Data Processing

Sections II-A to II-C have derived the Cramér-Rao bound in the estimation of the mean deformation velocity for simultaneous squinted acquisitions. It is therefore of interest to address the estimation problem to see if this bound can be achieved. As shown in [19], the estimation procedure can be done in two steps by first filtering the phases with the so-called Phase Linking algorithm and then performing the estimation of the velocities. Such is also the approach for simultaneous acquisitions, i.e., the phases of each stack are filtered first, and then the mean deformation velocity is estimated. Afterwards, the 3-D deformation is retrieved by solving (9). Summarizing, but for the filtering of the phases with Phase Linking, no

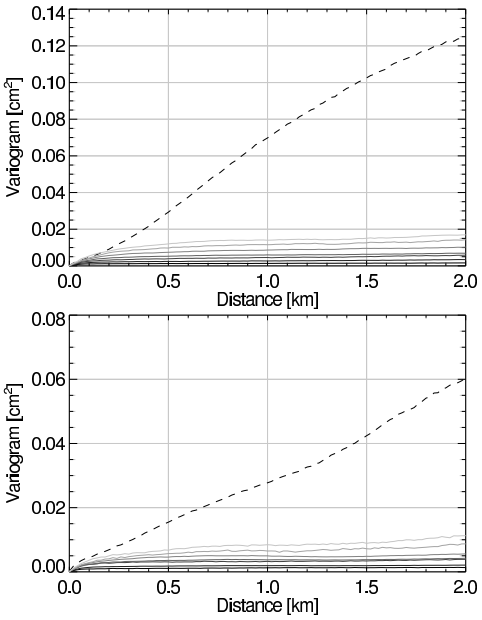

Fig. 4. Variograms of the interferograms and SD/MAI phases shown in Fig. 3 for the (top) ascending and (bottom) descending geometry. The dashed black line corresponds to the variogram of the interferometric phase, while the variograms for the SD/MAI phases are shown with solid lines ranging from (solid black) $\Delta\beta = 0.11^\circ$ to (lightest solid gray) $\Delta\beta = 4.28^\circ$.

special processing steps have to be added to achieve the bound. The next section validates the derived Cramér-Rao bounds by using Monte-Carlo simulations following the proposed processing approach.

III. Performance Evaluation

In this section, the performance in the retrieval of 3-D mean deformation maps with squinted acquisitions using the results of Section II is exemplified for different system configurations. Table II presents an overview of the parameters for the three systems that have been analyzed. For the sake of the example, an exponential model for the temporal decorrelation has been assumed, with τ as the time constant and γ_∞ as the persistent coherence term. The selected systems are based on current spaceborne SAR missions under investigation, namely, Tandem-L [7], SAOCOM-CS [8] and a potential Sentinel-1 companion satellite [9] for systems #1, #2 and #3, respectively. For the sake of the comparison and evaluation of the results, several parameters have been forced to be the same.

The IDL (Interactive Data Language) source code to produce the performance curves shown in this section can be downloaded from [39].

TABLE II
Performance evaluation with squinted systems.

Parameter	System #1	System #2	System #3
Wavelength	L-band	L-band	C-band
Slave operation	Monostatic	Bistatic	Bistatic
ABL height		700 m	
ABL speed, v_{bl}	10 m/s	–	–
σ_α		1 cm	
σ_{iono} [a]		0.5 cm	
γ_∞	0.2	0.2	0.05
Time constant τ [days]	60	60	40
Number of looks (N)		200	
Observation period		1 year	
Repeat-pass cycle		16 days	
Incidence angle		35 deg	
Heading		12° (equator)	
# Passes		1 Asc.&1 Desc.	

[a] For comparison purposes, the same value has been used for both frequency bands.

Fig. 5 shows the performance for the two L-band systems, while Fig. 6 shows the performance of the C-band system with and without the consideration of the ionosphere. Fig. 7 shows also the performance for the C-band system for the slant-range and azimuth components, again with and without ionosphere. The diamonds in all figures correspond to the result of the Monte-Carlo simulations (1000 realizations) following the processing approach described in Section II-F. The results agree well with the theoretical values. Some observations and comments are summarized in the following:

- The fact that the tropospheric component is correlated between the simultaneous acquisitions implies that their difference (roughly directed in along-track, and hence in the N-S direction) is practically insensitive to the APS power. On the other hand, the other two components are still affected, and therefore their performance degrades for increasing APS power.
- The ionospheric term has been assumed uncorrelated between the simultaneous acquisitions with a power of $0.5\mathrm{cm}^2$ (see Table II), so that, as opposed to the tropospheric term, it affects all geometries the same. Consequently, the performance for the N-S is worse than for the other two, and larger squint angles are required to obtain similar performances. Obviously, the ionospheric phase term is proportional to the inverse of the square of the central frequency, so that higher frequency bands will tend to be less affected. In any case, data-based correction approaches [29], [34] can be applied to mitigate the ionospheric phase noise.
- The performance is better for the quasi-simultaneous case (monostatic slave) than for the simultaneous case (bistatic slave). Although in the latter case the one-way APS of the master image cancels out in the difference interferogram, in the monostatic case the sensitivity to the motion is larger, i.e., a factor 4π instead of 2π for the second line of sight (cf. Fig. 5).
- A higher APS power will result in a closer performance of the three components, since the performance in the N-S direction remains practically unaffected, while the performance for the other two will degrade.
- The higher the frequency band, the better the performance

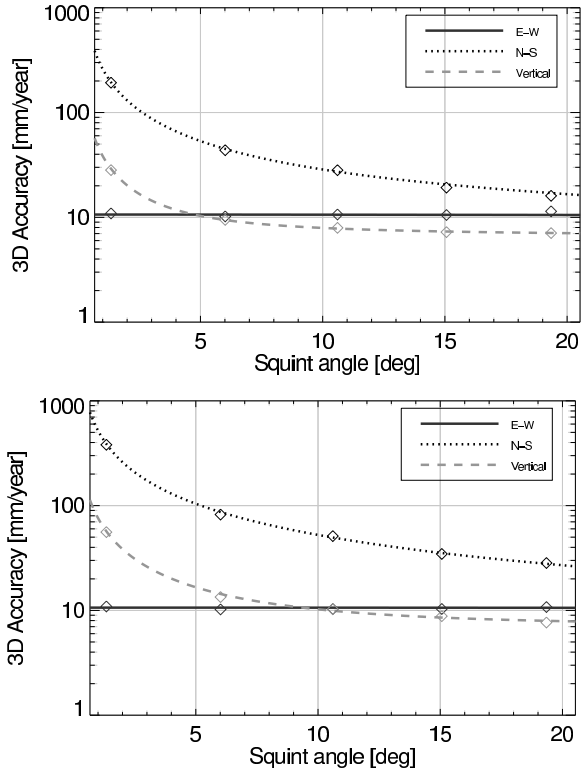

Fig. 5. Performance in the retrieval of the 3-D mean deformation velocity as a function of the geometric squint angle for systems (top) #1 and (bottom) #2. The diamonds correspond to the result of Monte-Carlo simulations.

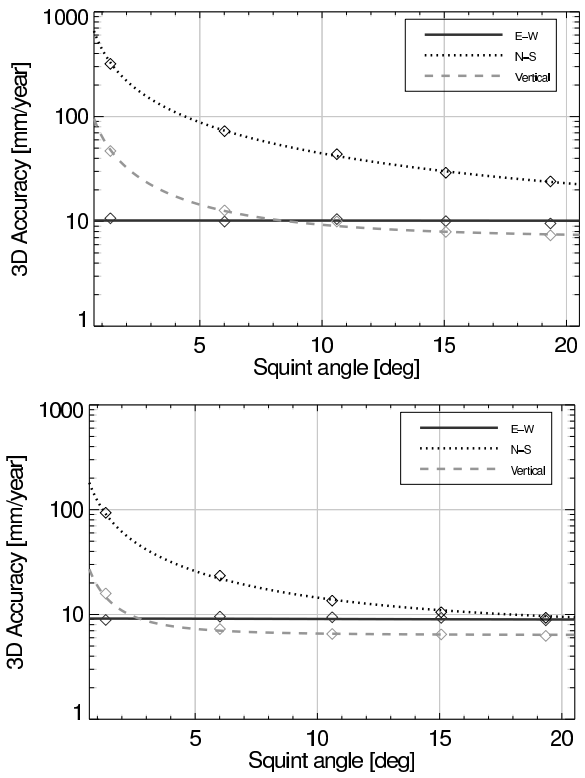

Fig. 6. Performance in the retrieval of the 3-D mean deformation velocity as a function of the geometric squint angle for system #3 (top) with and (bottom) without including the ionospheric component. The diamonds correspond to the result of Monte-Carlo simulations.

in the N-S direction, as the troposphere is almost canceled. As discussed in [40], the performance of differential SAR interferometry is frequency independent (with wavelengths up to 7 cm), as the sensitivity gain for shorter wavelengths is lost due to a higher atmospheric noise. However, the high correlation of the APS for simultaneous squinted acquisitions implies that higher frequency bands will have a better performance in the N-S direction than lower frequency bands.

The particular case of conventional DInSAR, i.e., with only two passes, is generally used for the study and evaluation of geophysical hazards like earthquakes and volcanic eruptions. Fig. 8 shows the performance evaluation as a function of the geometric squint angle for system #3 with two different temporal baselines, namely, 16 and 64 days. It becomes evident again that an increase of the squint angle improves the sensitivity to the N-S component of the motion. In the case no ionosphere is present, the benefit is evident. On the other hand, the presence of a residual ionospheric component strongly affects the retrieval of the azimuthal motion, which when performing the 3-D inversion, also impairs the retrieval of the vertical component. Note also that the performance is almost identical for the 16 and 64 day cases, as the uncertainty is dominated by the ionospheric noise.

Finally, note that the performance of the exploitation of the overlap area in burst modes, e.g., TOPS Sentinel-1 [41], or of 2-look burst modes [4], can be also evaluated using the presented tools, since in those cases also two different lines of

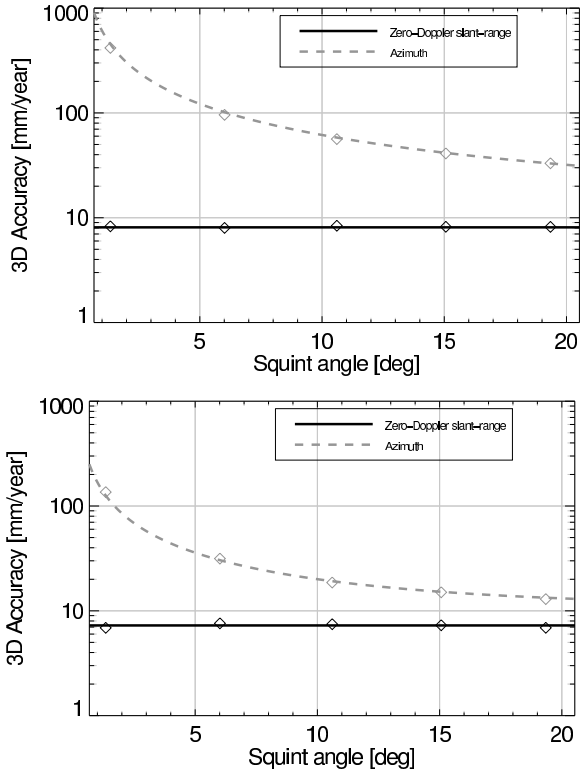

Fig. 7. Performance in the retrieval of the mean deformation velocity in the slant-range plane as a function of the geometric squint angle for system #3 (top) with and (bottom) without including the ionospheric component. The diamonds correspond to the result of Monte-Carlo simulations.

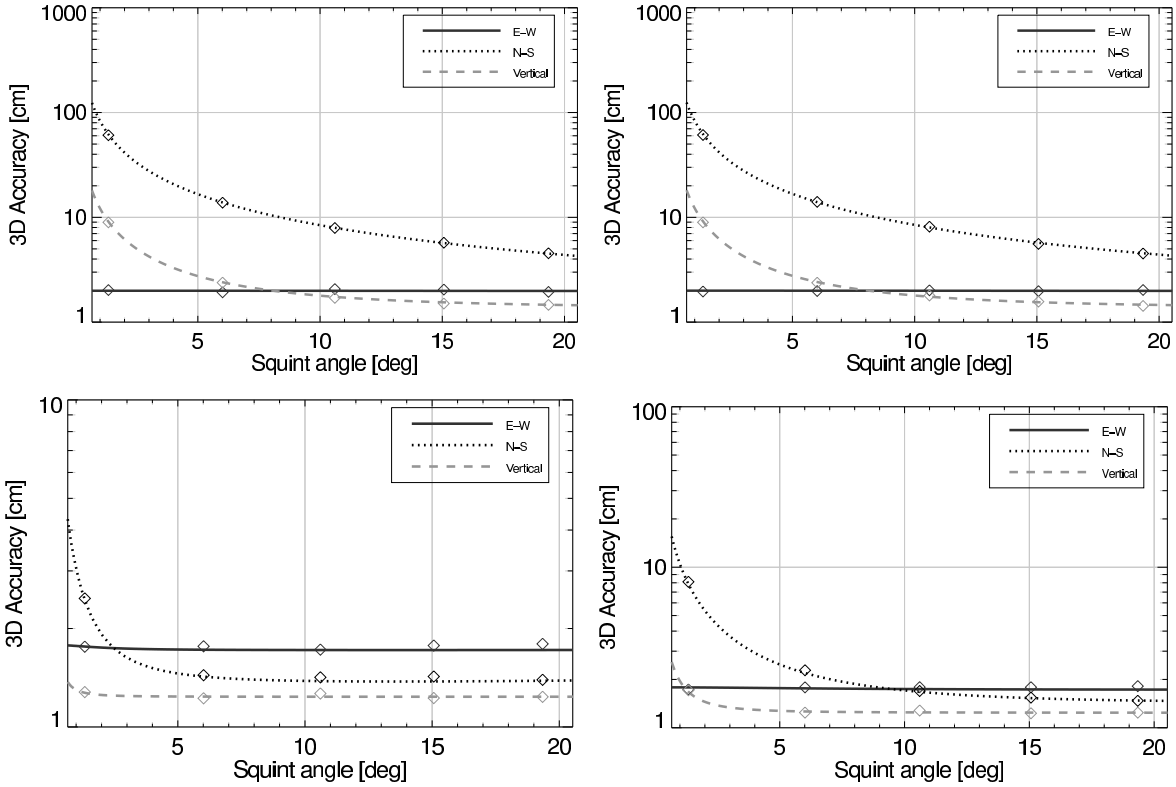

Fig. 8. Performance in the retrieval of the 3-D deformation as a function of the squint angle for system #3 with a two-passes scenario. Temporal baseline of (left column) 16 and (right column) 64 days assuming the exponential decorrelation model with the parameters shown in Table II and (top row) with and (bottom row) without ionosphere. The diamonds correspond to the result of the Monte-Carlo simulations.

sight are available. It is worth mentioning that in those cases, even if the angular separation between the lines of sight is small, one should be always careful with the interpretation of the SD/MAI phases, as they can be potentially contaminated by atmospheric noise, especially ionosphere.

IV. Conclusion

The use of large squint angles (lines of sight) to estimate the along-track deformation has been suggested in the frame of several spaceborne SAR missions. In practice, the exploitation of independent lines of sight is achieved when applying spectral diversity (aka MAI) with conventional acquisitions, where in this case the angular separation between the lines of sight is limited by the azimuth bandwidth (and hence the achievable performance is also limited by the azimuth resolution). For such small angular separations, the measurement of the motion in the along-track dimension remains practically unaffected by the tropospheric noise, as the lower part of the troposphere (atmospheric boundary layer, ABL) between the lines of sight is highly correlated. Such assumption is not valid for increasing angular separations. In order to address such cases, this paper has presented the mathematical framework to evaluate the performance in the retrieval of 3-D deformation maps when exploiting simultaneous or quasi-simultaneous interferometric acquisitions with different squint angles, by properly considering the correlation of the atmospheric delays between the acquisitions. The ABL has a high spatial correlation and is located close to the ground, implying that even for large angular separations the correlation between lines of sight, while not equal to one, will still be high. The presented quantitative analysis with TerraSAR-X staring spotlight data supports this assumption. As a consequence, simultaneous squinted acquisitions will allow a better sensitivity to the deformation in the N-S component when compared to the other two components (east and vertical), which are still affected by the troposphere. The performance will be better, the larger the angular separation between the lines of sight. On the other hand, the ionosphere might represent a limiting factor for low-frequency systems if not corrected, as in general it cannot be assumed to be correlated for the simultaneous acquisitions. The presented equations for both monostatic and bistatic systems have been validated with Monte-Carlo simulations, and have been used to evaluate three different scenarios based on spaceborne SAR missions currently under investigation.

Acknowledgments

The authors would like to thank Prof. Monti Guarnieri, Politecnico di Milano, for the discussions.

References

[1] T. Wright, B. Parsons, and Z. Lu, "Toward mapping surface deformation in three dimensions using InSAR," *Geophysical Research Letters*, vol. 31, no. 1, 2004.

[2] S. J. Frasier and A. J. Camps, "Dual-beam interferometry for ocean surface current vector mapping," *Geoscience and Remote Sensing, IEEE Transactions on*, vol. 39, no. 2, pp. 401–414, 2001.

[3] P. Lopez-Dekker, M. Rodriguez-Cassola, P. Prats, F. De Zan, T. Kraus, S. Sauer, and J. Mittermayer, "Experimental bidirectional SAR ATI acquisitions of the ocean surface with TanDEM-X," *Proceedings of EUSAR*, 2014.

[4] P. Prats-Iraola, M. Rodriguez-Cassola, N. Yague-Martinez, P. López-Dekker, R. Scheiber, F. D. Zan, T. Kraus, and s. Wollstadt, "Repeat-pass interferometric experiments with the Tandem-X constellation for accurate along-track motion estimation," in *2015 IEEE International Geoscience and Remote Sensing Symposium (IGARSS)*. IEEE, 2015, pp. 4077–4080.

[5] H.-S. Jung, Z. Lu, A. Shepherd, and T. Wright, "Simulation of the SuperSAR multi-azimuth synthetic aperture radar imaging system for precise measurement of three-dimensional Earth surface displacement," *IEEE Trans. Geosci. Remote Sens.*, vol. 53, no. 11, pp. 6196–6206, 2015.

[6] H. Ansari, F. D. Zan, A. Parizzi, M. Eineder, K. Goel, and N. Adam, "Measuring 3-D surface motion with future SAR systems based on reflector antennae," *IEEE Geosci. Remote Sens. Lett.*, vol. 13, no. 2, pp. 272–276, 2016.

[7] G. Krieger, A. Moreira, M. Zink, I. Hajnsek, S. Huber, M. Villano, K. Papathanassiou, M. Younis, P. L. Dekker, M. Pardini *et al.*, "Tandem-L: Main results of the phase a feasibility study," in *Geoscience and Remote Sensing Symposium (IGARSS), 2016 IEEE International*. IEEE, 2016, pp. 2116–2119.

[8] M. Davidson, N. Gebert, B. Carnicero Dominguez, F. Fois, and P. Silvestrin, "SAOCOM-CS: a passive companion mission to SAOCOM for single-pass L-band SAR bistatic interferometry and tomography," in *Proceedings of IGARSS 2014*, 2014, pp. 1–4.

[9] P. Lopez-Dekker, H. Rott, S. Solberg, M. Zonno, P. Prats, and A. Moreira, "SESAME (SEntinel-1 SAR Companion Multistatic Explorer) mission overview," in *Proceedings of FRINGE*, Helsinki, Finnland, Jun. 2017.

[10] J. Mittermayer, S. Wollstadt, P. Prats-Iraola, P. López-Dekker, G. Krieger, and A. Moreira, "Bidirectional SAR imaging mode," *IEEE Trans. Geosci. Remote Sens.*, vol. 51, no. 1, pp. 601–614, Jan. 2013.

[11] N. Bechor and H. A. Zebker, "Measuring two-dimensional movements using a single InSAR pair," *Geophysical research letters*, vol. 33, no. 16, 2006.

[12] S. Mancon, A. M. Guarnieri, D. Giudici, and S. Tebaldini, "On the phase calibration by multisquint analysis in TOPSAR and stripmap interferometry," *IEEE Trans. Geosci. Remote Sens.*, vol. 55, no. 1, pp. 134–147, 2017.

[13] R. Scheiber and A. Moreira, "Coregistration of interferometric SAR images using spectral diversity," *IEEE Trans. Geosci. Remote Sens.*, vol. 38, no. 5, pp. 2179–2191, Jul. 2000.

[14] R. Bamler and M. Eineder, "Accuracy of differential shift estimation by correlation and split-bandwidth interferometry for wideband and Delta-k SAR systems," *IEEE Geosci. Remote Sens. Lett.*, vol. 2, no. 2, pp. 151–155, Apr. 2005.

[15] F. D. Zan, P. Prats-Iraola, and M. Rodriguez-Cassola, "On the dependence of delta-k efficiency on multilooking," *IEEE Geosci. Remote Sens. Lett.*, vol. 12, no. 8, pp. 1745–1749, 2015.

[16] H.-S. Jung, J.-S. Won, and S.-W. Kim, "An improvement of the performance of multiple-aperture SAR interferometry (MAI)," *IEEE Trans. Geosci. Remote Sens.*, vol. 47, no. 8, pp. 2859–2869, 2009.

[17] H.-S. Jung, W.-J. Lee, and L. Zhang, "Theoretical accuracy of along-track displacement measurements from multiple-aperture interferometry (MAI)," *Sensors*, vol. 14, no. 9, pp. 17 703–17 724, 2014.

[18] A. Monti Guarnieri and S. Tebaldini, "Hybrid Cramér–Rao bounds for crustal displacement field estimators in SAR interferometry," *IEEE signal processing letters*, vol. 14, no. 12, pp. 1012–1015, 2007.

[19] ——, "On the exploitation of target statistics for SAR interferometry applications," *IEEE Trans. Geosci. Remote Sens.*, vol. 46, no. 11, pp. 3436–3443, 2008.

[20] A. Ferretti, C. Prati, and F. Rocca, "Permanent scatterers in SAR interferometry," *IEEE Trans. Geosci. Remote Sens.*, vol. 39, no. 1, pp. 8–30, Jan. 2001.

[21] R. F. Hanssen, F. van Leijen, N. Pierdicca, N. Floury, and U. Wegmuller, "L-band multistatic radar interferometry for 3D deformation vector decomposition," in *2015 IEEE International Geoscience and Remote Sensing Symposium (IGARSS)*. IEEE, 2015, pp. 4057–4060.

[22] H. L. Van Trees, *Detection, estimation, and modulation theory*. John Wiley & Sons, 2004.

[23] Y. Rockah and P. Schultheiss, "Array shape calibration using sources in unknown locations–part I: Far-field sources," *IEEE Transactions on Acoustics, Speech, and Signal Processing*, vol. 35, no. 3, pp. 286–299, 1987.

[24] R. F. Hanssen, *Radar Interferometry. Data Interpretation and Error Analysis*. The Netherlands: Kluwer Academic Publishers, 2001.

[25] F. Rocca, "Modeling interferogram stacks," *Geoscience and Remote Sensing, IEEE Transactions on*, vol. 45, no. 10, pp. 3289–3299, 2007.

[26] K. M. Chan and R. Wood, "The seasonal cycle of planetary boundary layer depth determined using COSMIC radio occultation data," *Journal of Geophysical Research: Atmospheres*, vol. 118, no. 22, 2013.

[27] A. N. Kolmogorov, "Dissipation of energy in locally isotropic turbulence," in *Dokl. Akad. Nauk SSSR*, vol. 32, 1941, pp. 19–21.

[28] G. I. Taylor, "The spectrum of turbulence," in *Proceedings of the Royal Society of London A: Mathematical, Physical and Engineering Sciences*, vol. 164, no. 919. The Royal Society, 1938, pp. 476–490.

[29] G. Gomba, A. Parizzi, F. D. Zan, M. Eineder, and R. Bamler, "Toward operational compensation of ionospheric effects in SAR interferograms: the split-spectrum method," *IEEE Trans. Geosci. Remote Sens.*, vol. 54, no. 3, pp. 1446–1461, 2016.

[30] J. Mittermayer, S. Wollstadt, P. Prats, and R. Scheiber, "TerraSAR-X staring spotlight with extended azimuth steering," *IEEE Trans. Geosci. Remote Sens.*, 2013.

[31] P. Prats-Iraola, R. Scheiber, M. Rodriguez-Cassola, J. Mittermayer, S. Wollstadt, F. D. Zan, B. Bräutigam, M. Schwerdt, A. Reigber, and A. Moreira, "On the processing of very high-resolution spaceborne SAR data," *IEEE Trans. Geosci. Remote Sens.*, vol. 52, no. 10, pp. 6003–6016, Oct. 2014.

[32] P. Prats and J. J. Mallorqui, "Estimation of azimuth phase undulations with multisquint processing in airborne interferometric SAR images," *IEEE Trans. Geosci. Remote Sens.*, vol. 41, no. 6, pp. 1530–1533, Jun. 2003.

[33] F. De Zan, P. Prats-Iraola, R. Scheiber, and A. Rucci, "Interferometry with TOPS: coregistration and azimuth shifts," in *Proceedings of EUSAR*, 2014.

[34] J. Kim, K. P. Papathanassiou, R. Scheiber, and S. Quegan, "Correcting distortion of polarimetric SAR data induced by ionospheric scintillation," *IEEE Trans. Geosci. Remote Sens.*, vol. 53, no. 12, pp. 6319–6335, 2015.

[35] G. Gomba, F. R. González, and F. D. Zan, "Ionospheric phase screen compensation for the sentinel-1 TOPS and ALOS-2 ScanSAR modes," *IEEE Trans. Geosci. Remote Sens.*, vol. 55, no. 1, pp. 223–235, 2017.

[36] P. Prats, R. Scheiber, A. Reigber, C. Andres, and R. Horn, "Estimation of the surface velocity field of the Aletsch glacier using multibaseline airborne SAR interferometry," *IEEE Trans. Geosci. Remote Sens.*, vol. 47, no. 2, pp. 419–430, 2009.

[37] A. Reigber, P. Prats, and J. J. Mallorqui, "Refined estimation of time-varying baseline errors in airborne SAR interferometry," *IEEE Geosci. Remote Sens. Lett.*, vol. 3, no. 1, pp. 145–149, Jan. 2006.

[38] M. Rodriguez-Cassola, S. V. Baumgartner, G. Krieger, and A. Moreira, "Bistatic TerraSAR-X/F-SAR spaceborne–airborne SAR experiment: description, data processing, and results," *IEEE Trans. Geosci. Remote Sens.*, vol. 48, no. 2, pp. 781–794, 2010.

[39] (2017) Software to compute the performance of 3-D surface deformation for simultaneous squinted SAR acquisitions. http://www.dlr.de/hr/software.

[40] F. Rocca, "Diameters of the orbital tubes in long-term interferometric SAR surveys," *IEEE Geosci. Remote Sens. Lett.*, vol. 1, no. 3, pp. 224–227, 2004.

[41] P. Prats-Iraola, R. Scheiber, L. Marotti, S. Wollstadt, and A. Reigber, "TOPS interferometry with TerraSAR-X," *IEEE Trans. Geosci. Remote Sens.*, vol. 50, no. 8, pp. 3179–3188, 2012.

Pau Prats-Iraola (S'03–M'06–SM'13) was born in Madrid, Spain, in 1977. He received the Ingeniero degree and the Ph.D. degree, both in telecommunications engineering, from the Universitat Politècnica de Catalunya (UPC), Barcelona, Spain, in 2001 and 2006, respectively.

In 2001, he was a Research Assistant at the Institute of Geomatics, Spain. In 2002, he was at the Department of Signal Theory and Communications, UPC, where he worked in the field of airborne repeat-pass interferometry and airborne differential SAR interferometry. From December 2002 to August 2006, he was an Assistant Professor at the Department of Telecommunications and Systems Engineering, Universitat Autònoma de Barcelona, Barcelona, Spain. In 2006, he joined the Microwaves and Radar Institute, German Aerospace Center (DLR), Wessling, Germany, where, since 2009, he has been the Head of the Multimodal Algorithms Group. His research interests include high-resolution airborne/spaceborne monostatic/bistatic SAR processing, SAR interferometry, advanced interferometric acquisition modes, Persistent Scatterer Interferometry (PSI), SAR tomography and end-to-end SAR simulation. He has co-authored about 50 peer-reviewed journal papers in the field.

Paco López-Dekker was born in Nijmegen, The Netherlands, in 1972. He received the Ingeniero degree in telecommunication engineering from Universitat Politècnica de Catalunya (UPC), Barcelona, Spain, in 1997, the M.S. degree in electrical and computer engineering from the University of California, Irvine, CA, USA, in 1998, under the Balsells Fellowship, and the Ph.D. degree from the University of Massachusetts, Amherst, MA, USA, in 2003, for his research on clear-air imaging radar systems to study the atmospheric boundary layer.

In 2003, he joined Starlab Barcelona, where he worked on the development of GNSS-R sensors and techniques. From 2004 to 2006, he was a Visiting Professor with the Department of Telecommunications and Systems Engineering, Universitat Autònoma de Barcelona. In March 2006, he was awarded a Ramon y Cajal Grant to conduct pioneering research on bistatic synthetic aperture radar (SAR) at Remote Sensing Laboratory, UPC. At the university, he taught courses on signals and systems, signal processing, communications systems and radiation, and guided waves.

Between November 2009 and August 2016, he led the SAR Missions Group at the Microwaves and Radar Institute, German Aerospace Center, Wessling, Germany. The focus of the group was the study of future SAR missions, including the development of novel mission concepts and detailed mission performance analyses. Since September 2016 he is Associate Professor at the Geoscience and Remote Sensing Department of the Faculty of Civil Engineering and Geosciences at the Delft University of Technology.

He has been deeply involved in several radar mission proposals, leading the Sentinel-1 SAR Multistatic Explorer (SESAME) mission proposal, and co-authored 30 peer-reviewed journal papers and over 100 conference contributions in a broad range of topics related to radar remote sensing.

Francesco De Zan was born in Lodi, Italy, in 1979. He studied Telecommunications Engineering at Politecnico di Milano (Italy) from 1998 to 2004, with a focus on signal processing and remote sensing. In 2008 he earned a PhD degree under the supervision of Prof. Fabio Rocca on Synthetic Aperture Radar (SAR) interferometry with distributed and decorrelating targets.

During the PhD he also contributed to the development of the TOPS acquisition mode, for which he was awarded at the 2006 EUSAR conference in Dresden with a student prize, and is currently used on European Space Agency (ESA) Sentinel-1 satellites. In 2007 he visited for two quarters the Stanford Exploration Group at Stanford University, California, which is specialized in the use of seismic waves to image the interior of the Earth. After the conclusion of his PhD, Francesco De Zan moved to the Munich area (Germany) to join the German Aerospace Center (DLR). He has worked first at the Microwave and Radar Institute, then at the Remote Sensing Technology Institute, contributing to the development of the Tandem-L mission concept. He has worked on aspects related to acquisition planning, performance models for deformation retrieval with InSAR and SAR tomographic applications, orbit design, and others. He was also involved in the calibration of the TanDEM-X interferometer, discovering and explaining a number of interferometric effects which were hampering the quality of the DEM products. Francesco De Zan has worked on several projects for ESA related to mission design, commissioning and application development for SAR satellites. His research interests in the field of SAR include performance of phase and delay estimators, ionospheric propagation estimation, focusing and precise geolocation of targets, soil moisture effects, inconsistencies in SAR interferometric phases. Francesco De Zan is a co-author of a few patents in the SAR field. He has given several introductory lessons at university level on SAR and SAR Interferometry and has supervised some master and PhD theses. He has participated at many international workshops and conferences and is the author/co-author of about 30 peer-reviewed publications in the field.

Néstor Yagüe Martínez received the Ingeniero degree in Telecommunication Engineering from the Universitat Politècnica de València (UPV), Valencia, Spain, in 2004.

From 2006 to 2015 he was with the Chair for Remote Sensing Technology, Technische Universität München (TUM), Munich, Germany, and also with the Remote Sensing Technology Institute, German Aerospace Center (DLR), Oberpfaffenhofen, Germany, where he worked in the development of the operational interferometric processor of the TanDEM-X mission. He spent a year from 2011 to 2012 at Starlab Barcelona S.L. working on along-track Interferometry for ocean surface currents retrieval. In 2015 he joined the Multimodal Algorithms Group, Microwaves and Radar Institute, DLR, Oberpfaffenhofen. His research interests include SAR processing, SAR interferometry, and differential SAR interferometry.

Mariantonietta Zonno was born in Bari, Italy, in 1986. She received the M.S. degree (with honor) in telecommunication engineering from Politecnico di Bari, Bari, in 2011 and the Ph.D. degree jointly from Scuola Interpolitecnica di Dottorato, Turin, Italy, and Politecnico di Bari, in March 2015.

During her Ph.D. studies, she visited the Microwaves and Radar Institute, German Aerospace Center (DLR), Wessling, Germany, for eight months. Since November 2014, she has been with the SAR Mission Group at the Microwaves and Radar Institute. Her major interests focus on the study future SAR missions concepts and analysis of the mission performance.

Marc Rodriguez-Cassola was born in Barcelona, Spain, in 1977. He received the Ingeniero degree in telecommunication engineering from Universidad Publica de Navarra, Pamplona, Spain, in 2000, the Licenciado (M.Sc.) degree in Economics from UNED, Madrid, Spain, and the Ph.D. in electrical engineering from the Karlsruhe Institute of Technology, Germany, both in 2012.

From 2000 to 2001, he was a radar hardware engineer at CETP/CNRS, Saint Maur des Fosses, France. From 2001 to 2003, he worked as a software engineer at Altran Consulting in Germany. Since 2003, he has been with the Microwaves and Radar Institute of the German Aerospace Center (DLR), where he is currently leading the SAR Missions group. His research interests encompass radar signal processing, SAR end-to-end simulation, SAR processing and calibration algorithms, crisis theory, radar mission analysis and applications.